12^{th} International Conference on Fracture Mechanics of Concrete and Concrete Structures
FraMCoS-12
B.L.A. Pichler, Ch. Hellmich, P. Preinstorfer (Eds)

https://doi.org/10.21012/FC12.1324
MS10-3:3

CALIBRATING A DAMAGE MODEL FROM LATTICE DISCRETE RESULTS

Julien Khoury*, Gilles Pijaudier-Cabot*, and Gianluca Cusatis †

* Université de Pau et des Pays de l'Adour, CNRS, Laboratoire des Fluides Complexes et leurs Réservoirs
Anglet 64600, France
e-mails: julien.khoury@univ-pau.fr and gilles.pijaudier-cabot@univ-pau.fr, www.univ-pau.fr

†Northwestern University, Department of Civil and Environmental Engineering
Evanston IL, 60208, USA
e-mail: g-cusatis@northwestern.edu, wwww.northwestern.edu

Key words: Lattice Discrete Particle Model, Continuum-based models, Coarse graining, Multiscale

Abstract. Lattice modeling of concrete is a discrete mesoscale representation of the material, where constitutive relations are prescribed at a smaller scale compared to traditional continuum-based models. These approaches can capture complex nonlinear behavior at the macroscale while maintaining a simpler and less phenomenological constitutive model at the mesoscale. Although these models come with a high computational cost, they are capable of accurately predicting global mechanical behavior and, in several cases, outperform continuum-based models. For this reason, they are considered valuable for generating high-fidelity databases that can be used in data-driven or coarse-graining approaches. In this study, discrete stress-strain findings from the Lattice Discrete Particle Model (LDPM) are upscaled using a coarse-graining technique based on the averaging of conservation equations. The results are used to calibrate a non-local damage model, where the non-local model's length is prescribed by the width of the area in which energy is dissipated in the LDPM calculations. Multiple coarse-graining lengths, ranging from one to five times the maximum aggregate size, are considered. We conclude that the non-local length should better be directly related to the width of the area where the energy is dissipated in the LDPM calculation. We also observe that the calibrated constitutive model provides consistent responses on other structural geometries, including size effect studies.

1 INTRODUCTION

Discrete and lattice models are widely used in the field of fracture mechanics (see the review in Ref. [4]). The Lattice Discrete Particle Model (LDPM) used in this study, is a good example of such models, where aggregates bigger than a certain size threshold are explicitly represented.

These models can accurately describe the mechanical response of geomaterials [1], but they come with a high computational cost. Alternative solutions should be considered, such as combining LDPM with classical finite elements [18]. Another approach is to homogenize the discrete results to obtain macro-scale continuum descriptions. These upscaled results can then be used in data-driven approaches or for calibrating an existing continuum model. One upscaling technique, suitable in the general case of nonlinear homogenization, is coarse-graining, where a continuous description is generated by applying conservation laws. In this study, LDPM results are homogenized using coarse graining with multiple coarse-graining lengths. The coarse-grained LDPM outputs are

then used for calibrating a non-local damage model. The calibrated model is validated using size effect calculations and by comparing the global responses of different geometries.

2 THE LATTICE DISCRETE PARTICLE MODEL (LDPM)

Originally developed by Cusatis and colleagues [5], the Lattice Discrete Particle Model (LDPM) is a mesoscale model designed to simulate particle interactions in granular materials, including mortar [15, 9], fiber-reinforced concrete, engineered cementitious composites [21, 20, 7, 22] and the cyclic behavior of concrete [24]. In this model, spherical particles representing the grain size distribution of the materials are arranged in the sample from the largest to the smallest size. A Delaunay tetrahedralization of the particle centers, along with nodes forming the external mesh, defines the lattice system. The domain is then tessellated, creating a network of polyhedral cells surrounding each spherical particle. The intersections of these cells are represented by triangular facets, where stresses and strains are expressed in vector form. Figure 1 provides an example of two adjacent polyhedral cells.

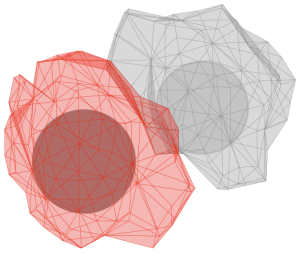

Figure 1: Polyhedral Cells Surrounding the LDPM Grains.

By incorporating a basic constitutive model at the mesoscale level, this model is highly accurate in predicting the behavior of granular materials, often outperforming traditional continuum-based models [1, 18]. For this reason, it is considered in this study as a high-fidelity model capable of generating a comprehensive database for data-driven approaches.

3 COARSE-GRAINING (CG)

The coarse-graining technique used in this contribution generates a continuous description of field quantities over the considered solid (stresses, strains, displacements) by manipulating conservation laws. Specifically, macroscale homogeneous constitutive relationships are derived from mesoscale heterogeneous LDPM findings.

The homogenized mass density is calculated by applying the convolution of the mass balance equation at the heterogeneous levels. The mass balance equations at both the heterogeneous and homogeneous levels, along with the mass density equation, are presented in equations (1), (2), and (3). In these equations, $\nabla.(x)$ represents the divergence of x, $(x)_\phi$ denotes the convolution of x, R is the mass density at the homogeneous level, ρ is the mass density at the heterogeneous level, and ϕ is the convolution function.

$$\frac{\partial \rho}{\partial t} + \nabla.(\rho v) = 0 \tag{1}$$

$$\frac{\partial R}{\partial t} + \nabla.(RV) = 0 \tag{2}$$

$$\frac{\partial R}{\partial t} = \frac{\partial \rho}{\partial t}_{\phi} = -\nabla.(\rho v)_\phi \tag{3}$$

For the convolution functions, the normalized Gaussian function shown in equation (4) is considered in this work, where L_{CG} is the coarse-graining length.

$$\phi(x,s) = \frac{1}{\frac{L_{CG}}{3}\sqrt{2\pi}} \exp\left\{ \left(\frac{-(x-s)^2}{2(\frac{L_{CG}}{3})^2} \right) \right\} \tag{4}$$

The homogenized velocity is determined from the mass balance equations at both levels. The upscaled velocity, as determined in equation (5), is computed as a function of the mesoscale velocity field v, the local mass density ρ, and the domain's coarse-grained mass density R. Homogenized displacements are then computed by integrating the velocity over time, as shown in equation (6), where U is the coarse-grained displacement.

$$V = \frac{(\rho v)_\phi}{R} \tag{5}$$

$$U = \int_t V dt = \int_t \frac{(\rho v)_\phi}{R} dt \tag{6}$$

Coarse-graining the balance of momentum at heterogeneous, meso-scale, level as represented in equation (7), and comparing it to the balance of momentum equation at the homogeneous level, as represented in equation (8), leads to equation (9), where σ represents the mesoscale stress field and S represents the macroscale or coarse-grained stress.

$$\frac{\partial \rho v}{\partial t} + \nabla.(\rho v \otimes v) = \nabla.(\sigma) \tag{7}$$

$$\frac{\partial RV}{\partial t} + \nabla.(RV \otimes V) = \nabla.(S) \tag{8}$$

$$\frac{\partial RV}{\partial t} = \frac{\partial (\rho v)_\phi}{\partial t} = (\nabla.(\sigma) - \nabla.(\rho v \otimes v))_\phi \tag{9}$$

Equations (10) and (11) can be directly determned from previous equation by introducing a fluctuating velocity $v' = v - V$.

$$\frac{\partial RV}{\partial t} + \nabla.(RV \otimes V) = (\nabla.(\sigma) - \nabla.(\rho v' \otimes v'))_\phi \tag{10}$$

$$S = (\sigma - (\rho v' \otimes v'))_\phi \tag{11}$$

The coarse-grained displacements and stresses at homogeneous levels are determined as a function of local entities in equations (6) and (11). As we are only dealing with quasi-static computations, the effect of fluctuating velocity is neglected, and the stress at the homogenized level is determined from local stresses as $S = (\sigma)_\phi$. Note that the angular momentum balance is not considered for upscaling in this study.

4 COARSE-GRAINING THE DISCRETE CALCULATIONS

Coarse-graining discrete results is not straightforward. LDPM results are defined by stress vectors at each facet and displacements at the center of each grain. Prior to proceeding with homogenization, a stress tensor at the center of each grain must to be estimated from the discrete results. Several approaches can be found in the literature to estimate an average stress tensor. Among the most well-known is the Love-Weber formula, which involves computing the tensor product between the contact force between particles and the vector joining the centers of the grains ([14, 23]). In this study, equation (12) is used for this purpose, where σ and ε are the stress and strain tensors, and n and t_k are the normal and stress vectors at each facet. Three uniaxial unit strain tensors and three unit shear strain tensors are imposed, and equation (12) is solved to estimate the stress tensor.

$$Find\ \sigma\ such\ that\ \forall \varepsilon \quad \sum_k [(\sigma.n - t_k).(\varepsilon^*.n)] = 0 \tag{12}$$

Five concrete notched beams, each measuring 700 mm in length, 200 mm in depth, and with a span-to-depth ratio of 2.5, are considered in this part. The notch thickness is 2 mm, and its length is 20% of the overall depth. The five distinct samples share the same parameters, differing only in their discrete particle distribution. A three-point bending LDPM calculation is then conducted for the five samples, and a grid of hexahedral elements, shown in Figure 2, with sizes ranging from $1/2.5D_{max}$ to less than $1/10D_{max}$, is considered for coarse-graining. In previous works (see e.g. [18]) the coarse-graining length L_{CG} was previously calibrated to represent a homogeneous behavior in the case of elasticity. In the present study, we shall consider multiple coarse-graining lengths, ranging from one to five times the maximum aggregate size.

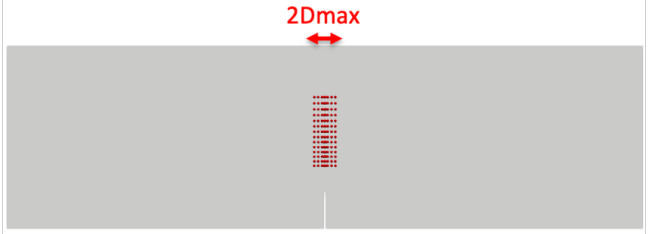

Figure 2: Coarse-graining points.

5 CALIBRATION OF A DAMAGE MODEL

In this section, the coarse-grained stresses and strains are used for the calibration of a continuous model. The model and equations below are defined by Mazars in Ref. [13], with a single modification: a non-local strain is used in this work. Concrete is assumed to be an isotropic, damageable material with a scalar damage parameter D. The constitutive relation is defined in equation (13) where σ is the second order stress tensor, ε is the second order strain tensor, C is the fourth order elastic stiffness tensor, and D is the damage scalar.

$$\sigma = (1 - D) \cdot C : \varepsilon \tag{13}$$

We also assume that the history parameter, described in equation (14) and denoted by $\mathbb{K}$, is driven by the non-local field of strains denoted by $\overline{\varepsilon}$, where K_{tr0} is the threshold of the damage.

$$\mathbb{K}(x,t) = max_{[0,t]}\ (\overline{\varepsilon}(x,t)\ ,\ K_{tr0}) \tag{14}$$

The non-local strain is described in equation (15):

$$\overline{\varepsilon} = \frac{\int \psi \tilde{\varepsilon} dv}{\int \psi dv} \tag{15}$$

where ψ is a Gaussian function with an internal length L_C and $\tilde{\varepsilon}$ is the equivalent strain defined in equation (16) with ε_i being the principal strains and $\langle x \rangle_+$ the Macauley bracket.

$$\tilde{\varepsilon} = \sqrt{\sum_{i=1}^{3} (\langle \varepsilon_i \rangle_+)^2} \tag{16}$$

Damage will not increase if $f(\tilde{\varepsilon}) < 0$ or $f(\tilde{\varepsilon}) = 0$ and $d\varepsilon \leq 0$. However, excessive tensile strain, such as $f(\tilde{\varepsilon}) = 0$ and $d\varepsilon > 0$, can cause damage. The evolution of damage in this model is described using equations (17) where $D_{t,c}$ determine the tensile and compressive damage parameters and α_t and α_c directly linked to the stresses.

$$g(\mathbb{K}) = \alpha_t \cdot D_t + \alpha_c \cdot D_c \tag{17}$$

Damage parameters are defined in equation (18):

$$D_{t,c} = 1 - \frac{K_{tr0}(1 - A_{t,c})}{\mathbb{K}} - \frac{A_{t,c}}{\exp^{B_{t,c}(\mathbb{K} - K_{tr0})}} \tag{18}$$

where $A_{t,c}$, $B_{t,c}$, and β are tensile, compressive and shear parameters respectively, which can be calibrated using uniaxial tensile or compressive testing. The parameters α_t and α_c are shown in equation (19), where $\varepsilon^{t,c}$ and $\sigma^{t,c}$ represent the tensile and compressive strains and stresses.

$$\begin{aligned} \alpha_t &= \sum_{i=1}^{3} \left(\frac{\langle \varepsilon_i^t \rangle \cdot \langle \varepsilon_i \rangle}{\tilde{\varepsilon}^2}\right)^{\beta} \\ \alpha_c &= \sum_{i=1}^{3} \left(\frac{\langle \varepsilon_i^c \rangle \cdot \langle \varepsilon_i \rangle}{\tilde{\varepsilon}^2}\right)^{\beta} \end{aligned} \tag{19}$$

$$\begin{aligned} \varepsilon^t &= (1 - D) \cdot C^{-1} : \sigma^t \\ \varepsilon^c &= (1 - D) \cdot C^{-1} : \sigma^c \end{aligned} \tag{20}$$

As shown in the previous equations, to compute D and $\mathbb{K}$ from coarse-grained results, an internal length L_C must be considered. This length is associated with the fracture process zone (FPZ) [3]. Because the non-local model should describe as accurately as possible the FPZ as obtained by LDPM, we will use the corresponding value for the internal length in the remaining part of this study. Note that this is at variance from the results by Pijaudier-Cabot et al. [19] where the internal length resulted from the calibration of the non-local damage model. The relationship between the internal length and the width of the FPZ is not explicit and the internal length must be determined by trial and error. Figure 4 shows the total energy dissipated at each grain from an LDPM calculation at one of the final time steps shown in Figure 3. At the same time step, Figure 5 shows the total energy dissipated in the LDPM calculation as well as the energy dissipated per unit volume in a non-local calculation with a length $L_C = 2D_{max}$ above the notch. It is this value of the internal length that will be used in the remaing part of this study.

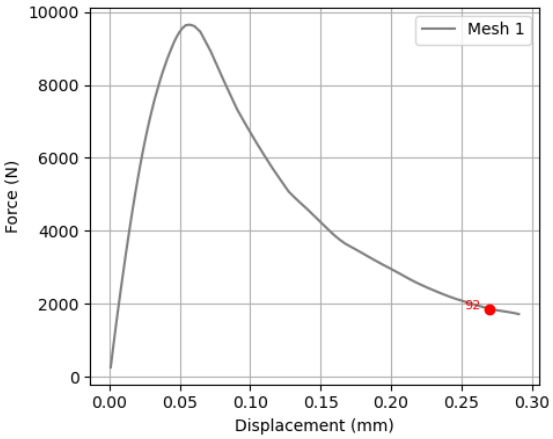

Figure 3: Time step 92 in the LDPM calculation.

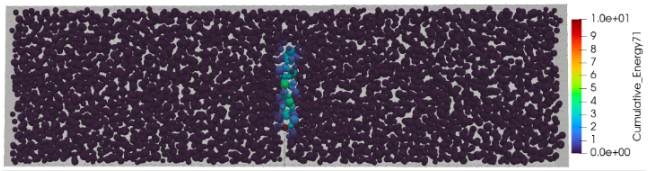

Figure 4: The dissipated energy at each grain at time step 92 in J.mm.

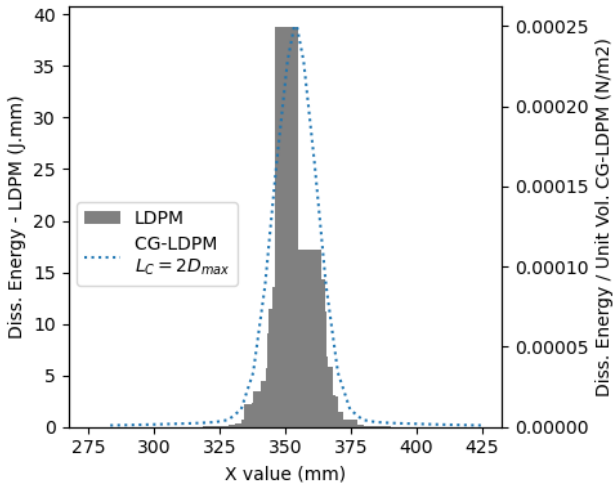

Figure 5: The dissipated energy from LDPM and non-local calculation with $L_C = 2D_{max}$.

After fixing the non-local length, we considered a varying coarse-graining length ranging from one to five times the maximum aggregate size. For each value of the coarse graining length, the non-local damage model has been calibrated (parameters A_t, B_t, and K_{tr0} in (18)) using the reconstructed relationship between D and $\mathbb{K}$ for each coarse grained stress-strain point, same as in Ref. [19] using the Levenberg-Marquardt procedure. The Sum of Squared Residuals (SSR) has been also computed to measure the difference between the D and $\mathbb{K}$ values obtained from the fitted non-local model and the coarse-grained data. Table 1 shows the evolution of the SSR with the variation of the coarse-graining length L_{CG}. The coarse graining length that minimizes the SSR defines he best posssible fit of the non-local model.

Table 1: SSR variation with the variation of L_{CG}

L_C	L_{CG}	SSR
$2D_{max}$	$1D_{max}$	1.468e-01
$2D_{max}$	$2D_{max}$	3.889e-02
$2D_{max}$	$3D_{max}$	3.577e-02
$2D_{max}$	$4D_{max}$	2.381e-02
$2D_{max}$	$5D_{max}$	2.941e-02

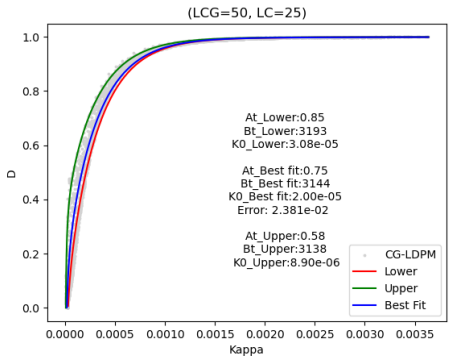

Figure 6: D vs. $\mathbb{K}$ plot for $L_{CG} = 4D_{max}$ and $L_C = 2D_{max}$ as well as the three non-local models

Having now the non-local and coarse-graining lengths, global calculations are conducted to compare results from the discrete and damage models.

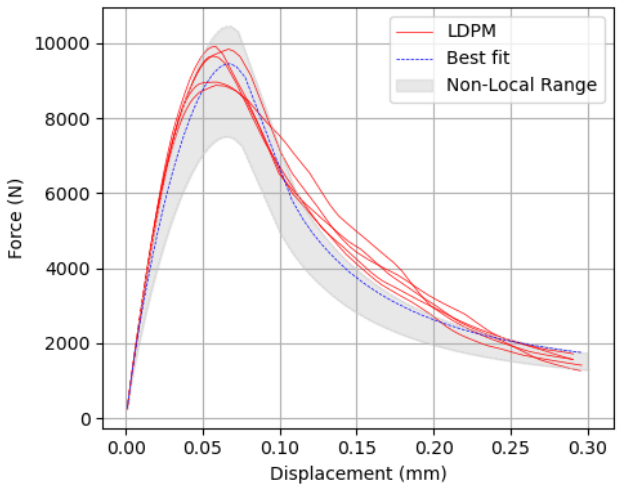

Figure 7: Range of non-local results

To capture all possible solutions, upper and lower bounds of the D–$\mathbb{K}$ plot are considered, with the corresponding fits of A_t, B_t, and K_{tr0}. Hence, three sets of non-local parameters are determined: two representing the extreme possibilities and one for the best fit. The D–$\mathbb{K}$ plots, as well as the three non-local model parameters, are shown in Figure 6, while the overall force-displacement result is shown in Figure 7. It is clear from Figure 7 that the range of non-local model results covers the LDPM findings, except for some points in the post-peak curve where the LDPM forces are slightly higher than the non-local ones.

6 VALIDATION

It is well established that LDPM captures size effects [16, 6, 12, 17, 8] and that a non-local model can describe size effect results of three-point bending tests on notched beams [11]. To validate our calibration, size effect tests will be simulated for the non-local damage model calibrated in the previous section and compared with LDPM results.

Three geometrically identical beams of varying sizes and a constant thickness of 50 mm are examined. The beam depths are 100 mm, 200 mm, and 400 mm, with a span-to-depth ratio of 2.5. All beams are notched with a notch thickness of 2 mm and a length-to-depth ratio of $1/5$. The LDPM parameters used in the previous section are considered here. All beams are shown in Figure 8, with larger beams shown in light grey in each figure for comparison.

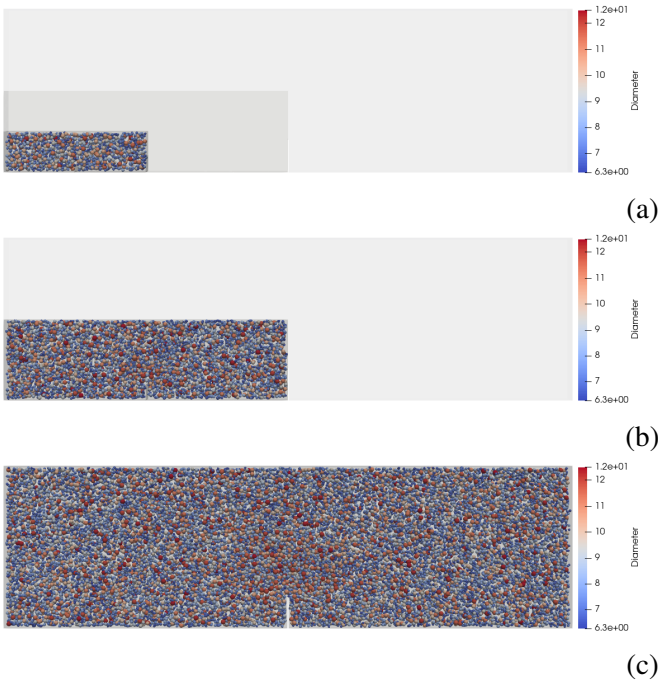

Figure 8: Identical beams for size effect calculations. Depths are (a) 100 mm, (b) 200 mm and (c) 400 mm

The results are analyzed using Bažant's side effect theory [2]. This method explores the connection between the nominal stress, σ_N, and the characteristic dimension, D, for geometrically similar specimens [10]. The proposed formula is outlined in equation (21) where, B represents a material property depending on the shape of the sample and the mechanical problem, f_t is the tensile strength, D is the sample's dimension, and D_0 is the characteristic dimension. The values of Bf_t and D_0 are obtained through linear regression in the form $Y = AX + C$, where $X = D$, $Y = (\frac{1}{\sigma_N})^2$, $Bf_t = \frac{1}{\sqrt{C}}$, and $D_0 = \frac{C}{A}$.

$$\sigma_N = \frac{Bf_t}{\sqrt{1 + \frac{D}{D_0}}} \tag{21}$$

The nominal stress σ_N is computed using simple beam formulas, shown in equation (22) where F is the maximum load, S is the span, b is the beam's width and D is the depth of the

beam. Results are shown in Figure 9. where $log(\frac{\sigma_N}{Bf_t})$ is plotted versus $log(\frac{D}{D_0})$.

$$\sigma_N = \frac{3}{2}\frac{FL}{b(0.8D)^2} \tag{22}$$

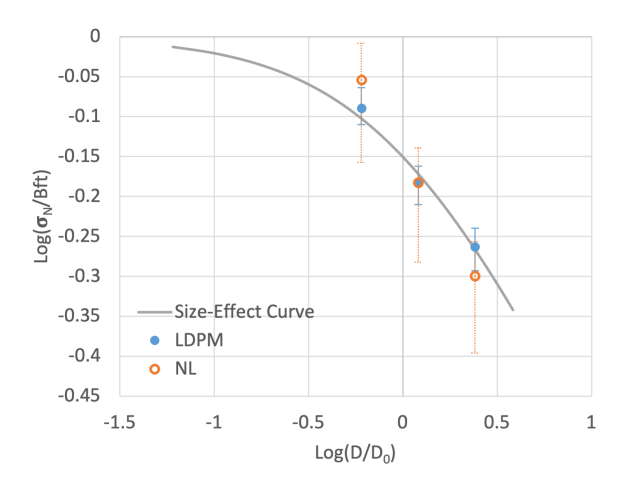

Figure 9: Size effect calculation

The inverse relationship between the material's strength and the beam size is clear, meaning that as the beam dimensions increase, the strength decreases. The strength reduction observed in the LDPM calculations appears to fall within the range of the strength reduction predicted by the non-local model.

Two other geometries are also considered for the validation of the non-local calibration: a notched cube and an L-shaped beam. Starting with the notched cube, the sample is subjected to uniform tensile stress, and results from LDPM and non-local calculations are compared. The cube is 400 mm in width and height, with a depth of 100 mm. The notch-to-width ratio is 1/5, with a notch thickness of 4 mm. The geometry and results are shown in Figure 10 and Figure 11.

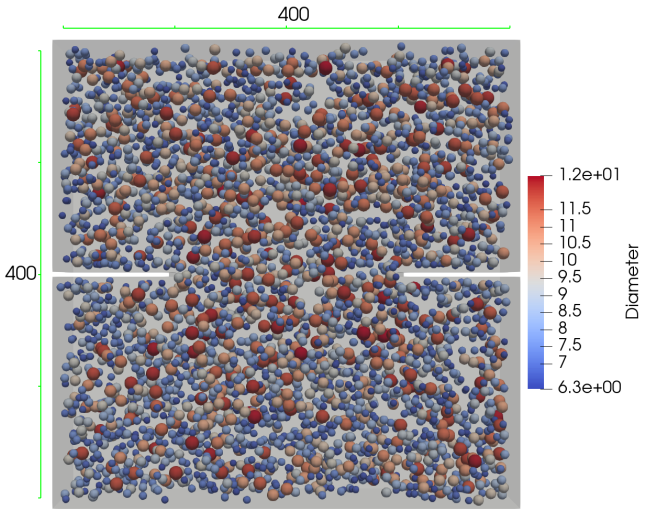

Figure 10: Notched Cube Geometry.

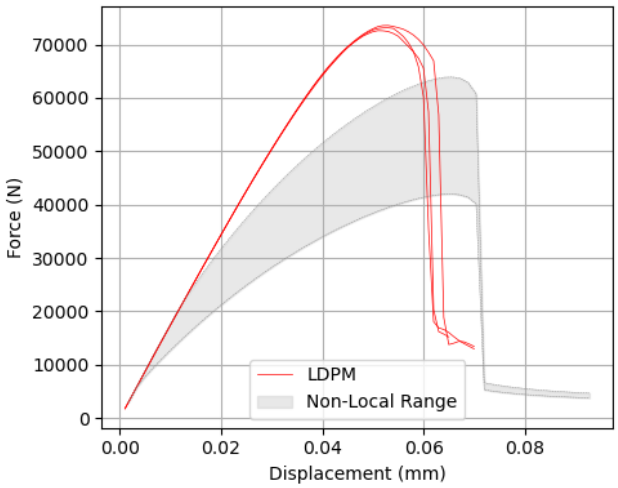

Figure 11: Notched Cube Calculation results.

The predicted non-local results do not match exactly with the LDPM calculations. The onset of non-linear behavior in the non-local model occurs earlier than in the LDPM results. This discrepancy is directly related to the K_{tr0} parameter, which influences the damage threshold in the non-local model. This threshold has a great influence on the computations and turns out to be the quantity with the largest variation on the fits that result from the D–$\mathbb{K}$ plot (upper, lower bounds and best fit). It is this quantity that is calibrated with the less confidence.

In a second series of validation examples, L-shaped samples are considered, with heights of

200 mm, 400 mm, 800 mm, and 1600 mm, and a constant depth of 50 mm. The samples are shown in Figure 14. These L-shaped samples are fixed at the bottom face and subjected to a vertical force from the side. The geometry, as well as the results from LDPM and non-local calculations for the 400 mm L-shaped samples, are shown in Figure 12 and Figure 13.

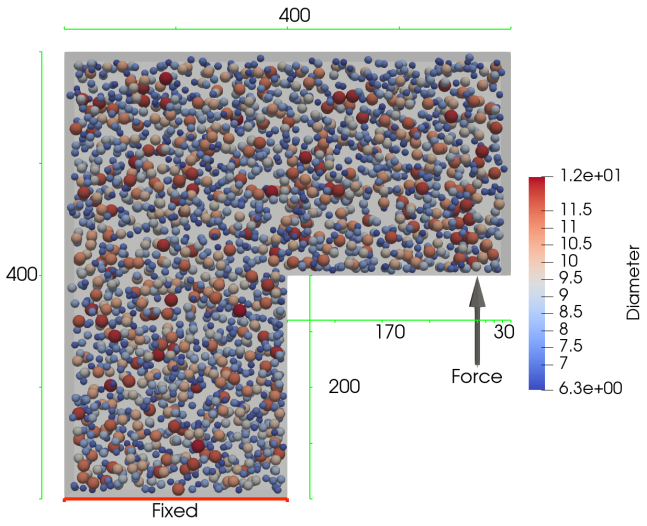

Figure 12: L-Shaped speciment Geometry.

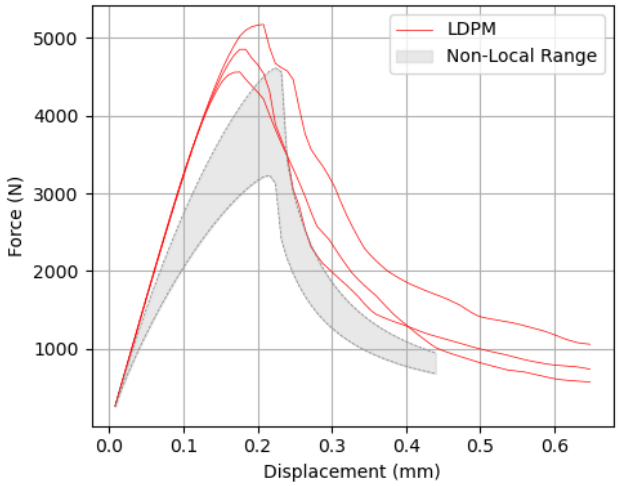

Figure 13: L-Shaped speciment calculation results

Similar to the notched cube observations, the predicted non-local range of results for the L-shaped beam falls within the same magnitude as the LDPM calculations. However, they do not match, with the primary difference being again the damage threshold. Size effect calculations are also performed for these samples.

Bažant's size effect law is also fitted for the L-shaped specimens. The size effect is fitted from LDPM calculations and the prediction from the non-local model is compared to the fit. Results are shown in Figure 14 and Figure 15.

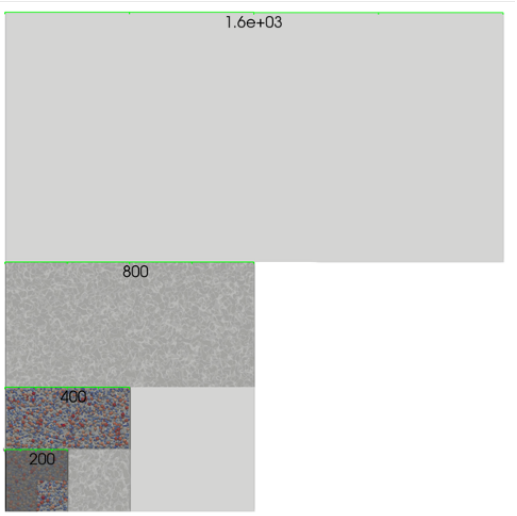

Figure 14: L-Shaped samples.

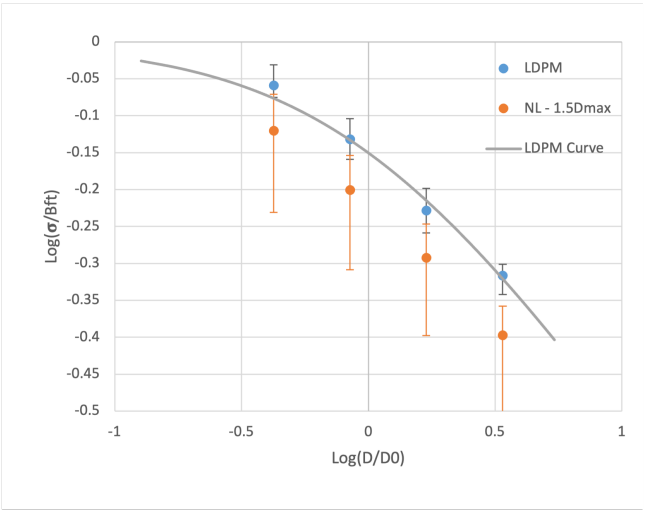

Figure 15: Size effect calculations for L-Shaped speciment

The nominal stresses obtained from LDPM calculations are slightly higher than those predicted by the non-local model. The results also indicate that the non-local model produces a

size effect curve that is shifted. A consistent shift suggests that the model introduces a similar magnitude of error across all sizes, meaning that the non-local model does not provide an incorrect description of size effect, which is biased whatever the specimen size, but the the model is probably too simple to capture the response of L-shaped specimen properly, being fitted on another geometry of fracture test.

7 CONCLUSIONS

Lattice calculations can provide high-fidelity mechanical responses of geomaterials ([1]). Homogenized results can be used either for the calibration of continuum models or in a data-driven approach. In this work, coarse graining LDPM model responses is employed with coarse graining lengths varying from one to five time the maximum aggregate size. The CG-LDPM results are then used to calibrate a non-local damage model with an internal length calibrated from the width of the fracture process zone obtained in the LDPM calculation. The Sum of Squared Residuals of the difference between the D and $\mathbb{K}$ values obtained from the fitted non-local model and the coarse-grained data is then computed and the coarse-graining length that minimizes the SSR is considered.

We observed a wide range of possible non-local results, primarily due to the sensitivity of the constitutive equations in this model. Although the LDPM results fall within the non-local calculations for the notched beam, we noticed that the results for different geometries falls within the same order of magnitude as the LDPM calculations, but they do not match. The main difference is the onset of the non-linear behavior, which is controlled by K_{tr0} in the non-local model and hard to fit with sufficient accuracy. We believe also that the damage model used is too simple to fully capture the global behavior of quasi-brittle materials, and its calibration remains dependent on the specimen's geometry.

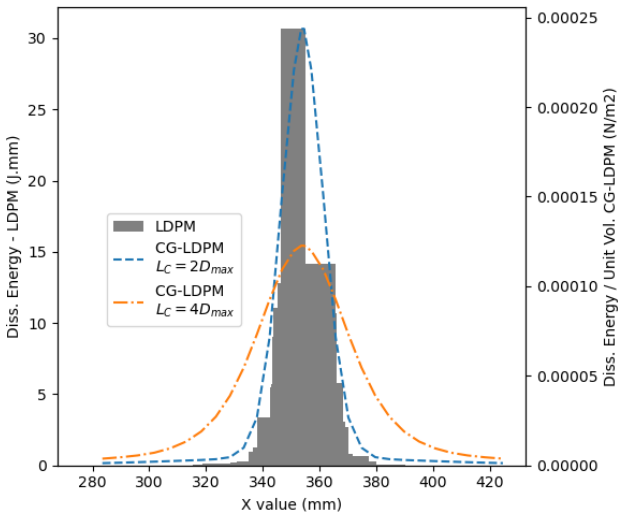

Figure 16: The dissipated energy from LDPM and two non-local calculations with $L_C = 2D_{max}$ and $L_C = 4D_{max}$.

It might also be important to compare the energy dissipation curves from an LDPM calculation with those from the current non-local model, calibrated using $L_{CG} = 4D_{max}$ and $L_C = 2D_{max}$, as well as from the non-local model calibrated in previous works with $L_{CG} = 4D_{max}$ and $L_C = 4D_{max}$ [19]. The current model better represents the width of the fracture process zone (FPZ) observed in the LDPM calculation, and at the same time the fit of the LDPM response of bending beams turns out to be more accurate. Therefore, it is important to constrain the size of the FPZ predicted by the non-local model to match with LDPM results instead of relying solely on the fits of stress-strain histories.

Although promising results have been found in this work, as mentioned previously, we believe the model used cannot capture complex behavior of quasi-brittle materials. Several improvements could be proposed, including but not limited to adding additional physical parameters, which would enhance the model's accuracy. Nevertheless, we think that applying CG-LDPM results in a data-driven approach is more promising, as this would eliminate the need for a macroscopic material model.

8 ACKNOWLEDGMENTS

Partial financial support from the investissement d'avenir French programme (ANR-16-IDEX- 0002), the European Union's Horizon 2020 research and innovation programme EDENE under the Marie Skłodowska-Curie grant agreement No 945416, and from the Communauté d'Agglomération Pau – Béarn – Pyrennées are gratefully acknowledged. This research was performed in part within the E2S hub Newpores supported jointly by Université de Pau et des Pays de l'Adour and Northwestern University.

REFERENCES

[1] Ashari, S. E., Buscarnera, G., & Cusatis, G. (2017). A lattice discrete particle model for pressure-dependent inelasticity in granular rocks. *International Journal of Rock Mechanics and Mining Sciences* **91**:49–58.

[2] Bažant, Z. P., & Planas, J. (2019). *Fracture and size effect in concrete and other quasibrittle materials.* Routledge.

[3] Bažant, Z. P., & Pijaudier-Cabot, G. (1989). Measurement of characteristic length of nonlocal continuum. *Journal of Engineering Mechanics* **115(4)**:755–767.

[4] Bolander, J. E., Eliáš, J., Cusatis, G., & Nagai, K (2021). Discrete mechanical models of concrete fracture. *Engineering Fracture Mechanics* **257**:108030.

[5] Cusatis, G., Pelessone, D., & Mencarelli, A. (2011). Lattice discrete particle model (ldpm) for failure behavior of concrete. i: Theory. *Cement and Concrete Composites* **33(9)**:881–890.

[6] Feng, J., Sun, W.-w., & Li, B.-m. (2018). Numerical study of size effect in concrete penetration with LDPM. *Defence Technology* **14**:560–569.

[7] Feng, J., Sun, W., Chen, L., Chen, B., Arkin, E., Du, L., & Pathirage, M. (2022). Engineered Cementitious Composites using Chinese local ingredients: Material preparation and numerical investigation. *Case Studies in Construction Materials* **16**:e00852.

[8] Grassl, P., Grégoire, D., Solano, L. R., & Pijaudier-Cabot, G. (2012). Meso-scale modelling of the size effect on the fracture process zone of concrete. *International Journal of Solids and Structures* **49(13)**:1818–1827.

[9] Han, L., Pathirage, M., Akono, A.-T., & Cusatis, G. (2021).Lattice discrete particle modeling of size effect in slab scratch tests. *Journal of Applied Mechanics* **88(2)**:021009.

[10] Haidar, K., Pijaudier-Cabot, G., Dubé, J.-F., & Loukili, A. (2005). Correlation between the internal length, the fracture process zone and size effect in model materials. *Materials and structures* **38**:201–210.

[11] Le Bellégo, C., Dubé, J. F., Pijaudier-Cabot, G., & Gérard, B. (2003). Calibration of nonlocal damage model from size effect tests. *European Journal of Mechanics-A/Solids* **22(1)**:33–46.

[12] Li, W., Zhou, X., Carey, J. W., Frash, L. P., & Cusatis, G. (2018). Multiphysics lattice discrete particle modeling (M-LDPM) for the simulation of shale fracture permeability. *Rock Mechanics and Rock Engineering* **51**:3963–3981.

[13] Mazars, J. (1986). A description of micro- and macroscale damage of concrete structures. *Engineering fracture mechanics* **25(5-6)**:729–737.

[14] Nicot, F., Hadda, N., Guessasma, M., Fortin, J., & Millet, O. (2013). On the definition of the stress tensor in granular media. *International Journal of Solids and Structures* **50(14-15)**:2508–2517.

[15] Pathirage, M., Bousikhane, F., D'ambrosia, M., Alnaggar, M., & Cusatis, G. (2019).Effect of alkali silica reaction on the mechanical properties of aging mortar bars: Experiments and numerical modeling. *International Journal of Damage Mechanics* **28(2)**:291–322.

[16] Pathirage, M., Tong, D., Thierry, F., Cusatis, G., Grégoire, D., & Pijaudier-Cabot, G. (2022). Numerical modeling of concrete fracturing and size-effect of notched beams. *Computational Modelling of Concrete and Concrete Structures*; pp. 496-502.

[17] Pathirage, M., Tong, D., Thierry, F., Cusatis, G., Grégoire, D., & Pijaudier-Cabot, G. (2023). Discrete modeling of concrete failure and size-effect. *Theoretical and Applied Fracture Mechanics* **124**:103738.

[18] Pijaudier-Cabot, G., & Khoury, J. (2024). Damage Mechanics for Quasi-Brittle Materials: Continuum and Lattice Descriptions. *Reference Module in Materials Science and Materials Engineering.*

[19] Pijaudier-Cabot, G., Khoury, J., Cusatis, G., Lattice and continuum damage modeling for fracture of concrete, Proc. FaMCoS 12, B.A. Pichler et al. (eds), (2025)

[20] Rezakhani, R., Scott, D. A., Bousikhane, F., Pathirage, M., Moser, R. D., Green, B. H., & Cusatis, G. (2021). Influence of steel fiber size, shape, and strength on the quasi-static properties of ultra-high performance concrete: Experimental investigation and numerical modeling. *Construction and Building Materials* **296**:123532.

[21] Schauffert, E. A., & Cusatis, G. (2012). Lattice discrete particle model for fiber-reinforced concrete. I: Theory. *Journal of Engineering Mechanics* **138(7)**:826–833.

[22] Smith, J., & Cusatis, G. (2017). Numerical analysis of projectile penetration and perforation of plain and fiber reinforced concrete slabs. *International Journal for Numerical and Analytical Methods in Geomechanics* **41(3)**:315–337.

[23] Wan, R., Duriez, J., & Darve, F. (2015). A tensorial description of stresses in triphasic granular materials with interfaces. *Geomechanics for Energy and the Environment* **4**:73–87.

[24] Zhu,Z., Pathirage,M., Wang,W., Troemner,M., &Cusatis,G. (2017). Lattice discrete particle modeling of concrete under cyclic tension–compression with multi-axial confinement. *Construction and Building Materials* **352**:128985.